Highly thermally stable epitaxial high-entropy fluorite oxide thin films

Jun Zhou[1,2], Nancy Lai Mun Wong[2], Hui Ru Tan[2], Ming Lin[2], Fengxia Wei[2], Ping Yang[3], Siao Li Liew[1,2], Jianwei Chai[2], Andrew Chun Yong Ngo[1,2], Shijie Wang[1,2,a)]

AFFILIATIONS

[1] Future Energy Acceleration & Translation (FEAT), Strategic Research & Translational Thrust (SRTT), A*STAR Research Entities, 1 Fusionopolis Way #20-10 Connexis North Tower, Singapore 138632, Republic of Singapore

[2] Institute of Materials Research and Engineering (IMRE), Agency for Science, Technology and Research (A*STAR), 2 Fusionopolis Way, Innovis #08-03, Singapore 138634, Republic of Singapore

[3] Singapore Synchrotron Light Source (SSLS), National University of Singapore (NUS), Singapore 117603, Republic of Singapore

a) Author to whom correspondence should be addressed: sj-wang@imre.a-star.edu.sg

ABSTRACT

While high-entropy fluorite oxides have shown promise for applications in extreme environments, achieving epitaxial integration with high thermal stability and structural coherence remains a significant challenge. Here, we report the synthesis of an epitaxial chemically disordered single-phase fluorite oxide thin film, (HfZrCeGdCa)O_2, on a YSZ (100) substrate via pulsed laser deposition. Structural characterization by X-ray diffraction (XRD) and atomic-resolution scanning transmission electron microscopy imaging and energy-dispersive X-ray spectroscopy confirm the high crystalline quality and uniform elemental distribution of the film, validating its chemically disordered single-phase character. In-situ temperature-dependent XRD shows the high thermal stability without phase separation and secondary phase formation up to 1200 °C. Reciprocal space mapping and strain analysis indicate coherent in-plane lattice matching with the YSZ substrate, accompanied larger out-of-plane lattice constant. Local lattice tilting, rotation, and interfacial dislocations are observed, suggesting partial strain relaxation close to the interface. These results underscore the structural integrity and thermal robustness of chemically disordered single-phase fluorite oxide films, supporting their potential use in advanced functional coatings for extreme environments.

High-entropy materials represent a cutting-edge class of materials, which as the name suggested, relies on the entropy, rather than the enthalpy in conventional materials, to stabilize the system. [1] To achieve high entropy, multiple elements (typically four or more) are mixed in (near-)equimolar concentrations and form a single-phase solid solution.[2,3] This design strategy leads to a range of unique features in high entropy materials.[4] For example, the random distribution of multiple cations in the lattice creates diverse diffusion barriers, resulting in sluggish diffusion. This heterogeneous and rugged potential energy surface significantly impedes the mobility of irradiation-induced point defects and clusters, contributing to radiation and corrosion resistance behavior.[5,6] Moreover, severe lattice distortion causes phonon broadening during irradiation cascades, reducing thermal conductivity while enhancing defect recombination.[7] Furthermore, the entropy-stabilized phase provides high thermal stability, enabling these materials to maintain structural integrity and resist melting or degradation under extreme temperatures. High-entropy materials also benefit from solid-solution strengthening and refined microstructures, improving their mechanical properties such as hardness, strength, and toughness. These attributes reduce the risk of thermally induced mechanical failure, ensuring long-term reliability in harsh environments.[8] Additionally, high-entropy materials offer compositional tunability, allowing for precise control over properties like the coefficient of thermal expansion (CTE) to match various substrates. This reduces the likelihood of delamination, cracking, and thermal mismatch stresses—enhancing coating performance and durability.

Due to these outstanding features, high-entropy materials have shown promise in a broad range of applications, including batteries, catalysts, structural materials for nuclear reactors, and thermal barrier coatings (TBCs).[6,7,9-12] Since the first report of high-entropy alloys, the concept has rapidly expanded to ceramics, with high-entropy ceramics (HECs) attracting significant attention. [13-20] And various high-entropy ceramic systems have been reported, including silicides, rocksalt oxides, perovskites, pyrochlores, and MXenes, to name a few.[1,21-23]

High-entropy oxides with a fluorite structure are among the most widely studied high-entropy oxide systems.[24,25] Several exploratory studies have reported the synthesis of dense epitaxial films by pulsed laser deposition (PLD).[26,27] One particularly interesting class of high-entropy fluorite oxides is the Zr-based compositional space, which can be regarded as “high-entropy analogues” of yttria-stabilized zirconia (YSZ).[28] YSZ is currently the state-of-the-art TBC material for gas turbine engines.[29] However, YSZ suffers from limitations, such as poor phase stability and sintering resistance at high temperatures, as well as relatively high thermal conductivity (around 1.8 W/mK at 950 °C), which restricts its performance in next-generation high-efficiency engines. Recent studies have shown that high-entropy fluorite oxides can overcome many of these limitations, offering reduced thermal conductivity, enhanced thermal stability, tunable CTEs, improved fracture toughness, and comparable hardness.[28,30-34] These results suggest strong potential for high-entropy fluorite oxides as advanced TBCs. However, all these findings are based on bulk samples, and it has shown that the properties of high-entropy oxide might change significantly in a coating form.[35]

A critical first step is to determine whether thin films fabricated from these Zr-based materials maintain the high-entropy phase. In this study, we extend our work from bulk high-entropy fluorite oxides to thin films deposited on YSZ (100) substrates using pulsed laser deposition (PLD), using $(HfZrCe)_{0.25}(GdCa)_{0.125}O_{2-\delta}$ as an example. Following our previous work, $(HfZrCe)_{0.25}(GdCa)_{0.125}O_{2-\delta}$ is denoted as 'GdCa' throughout this paper.[32] We systematically investigate their crystalline structure, composition, elemental distribution, and strain effects. These insights are crucial for advancing the application of high-entropy fluorite oxides in functional coatings, especially for high-performance thermal barrier coatings.

$(HfZrCe)_{0.25}(GdCa)_{0.125}O_{2-\delta}$ thin films were deposited on YSZ (100) substrates using PLD. A ceramic target of the same composition was synthesized via solid-state reaction of binary oxide nanopowders. Commercial YSZ (100) substrates were ultrasonically cleaned in acetone, ethanol and deionized water for 10 minutes to remove surface particles and contaminants, followed by drying with a nitrogen stream. Film deposition was carried out at 720 °C under an oxygen pressure of 3.9×10^{-2} mbar by oxygen flow of 1.75 sccm, which was determined as the optimal condition. A KrF excimer laser (248 nm, 25 ns) was used for target ablation at a pulse energy of 300 mJ and repetition rate of 10 Hz. The laser fluence is around 4.25 J/cm^2 and produced spot size is ~7 mm^2. The target-substrate distance is 10cm. These lead to a growth rate of around 7 nm/min. After deposition, the film was cooled down to room temperature under the same oxygen pressure to prevent further oxygen vacancy formation. Synchrotron-based X-ray diffraction experiments for reciprocal space mapping (RSM) were performed at room temperature using the X-ray Diffractometry and Demonstration (XDD) beamline at the Singapore Synchrotron Light Source (SSLS). Atomic-resolution HAADF-STEM imaging was performed on an aberration-corrected ThermoFisher Scientific Spectra 300 TEM operating at 200 kV. It is equipped with a Dual-X EDS detector and an S-CORR probe corrector. 4D STEM was operated at STEM microprobe mode with a convergence angle of ~ 0.5 mrad and a 50 μm aperture. Diffractions were acquired by STEMx using a GIF camera at 38 mm camera length. Large-area strain mapping was conducted using 4D-STEM data sets. The 4D-STEM data were acquired with Gatan DigitalMicrograph software, with the TEM operated in STEM microprobe mode using a 50 μm condenser aperture. The convergence angle is ~0.5 mrad. The scan area comprised 200 × 200 probe positions with a step size of 1.1 nm, yielding a total of 40,000 diffraction patterns. Diffraction patterns were collected by STEMx using a Gatan GIF camera at a camera length of 38 mm. The measured lattice strain variation (~2%) is consistent with the HRXRD results. Cross-sectional TEM lamellae of films were prepared using a focused ion beam (FIB, FEI Helios Nanolab 600). In-situ XRD was performed on a Bruker D8 Advance diffractometer equipped with Cu Kα radiation, a position-sensitive detector, and an Anton Paar heating stage to evaluate the thermal phase stability of the films. The samples were heated at a rate of 5 ˚C/min in air, and temperature was equilibrated for 2 mins at each temperature before data collection started. All data were collected over a 2θ range of 10° to 90°, with a step size of 0.02° and an exposure time of 0.1 s per step with a Cu absorber. Rietveld refinements were conducted using the TOPAS v5 software in batch mode, employing the fundamental parameters approach. The interlayer spacings were calculated using Bruker Eva software according to Bragg's Law. The CTE was estimated using a linear fitting of the interlayer spacing as a function of temperature.

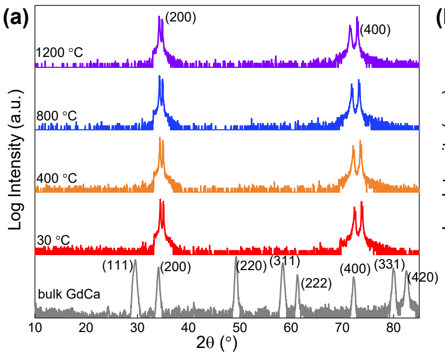

FIG. 1. Temperature dependent in-situ XRD patterns in a logarithmic scale for high-entropy GdCa film on YSZ (100) substrate with the bulk GdCa as reference in (a) full range and (b) range of 30° to 40°.

Figure 1 shows the temperature-dependent X-ray diffraction (XRD) patterns of the GdCa thin film deposited on a YSZ (100) substrate. The wide-range θ–2θ scans reveal two sets of peaks centered around 35° and 72°, corresponding to the (200) and (400) reflections, respectively. These two peaks align well with that of the bulk GdCa. A pair of closely spaced peaks originating from the GdCa film and the YSZ substrate can be observed, indicating that the two materials share the same crystal structure but slightly different lattice constants. The YSZ peaks appear at higher diffraction angles, suggesting it has smaller lattice constants than that of the GdCa film. No additional reflections corresponding to the secondary phases were observed, which is confirmed by the XRD in the zoomed-in view around 002 peak [see Figure 1(b)]. These results reveal the formation of a single-phase cubic fluorite structure in both the thin film and the substrate.

At room temperature, the (200) and (400) diffraction peaks for the GdCa thin film are located at 34.5° and 72.4°, respectively—slightly higher than those of bulk GdCa, which are reported at 34.1° and 72.0°.[32] This shift indicates a slightly smaller out-of-plane lattice parameter for the single-crystalline film (~5.20 Å) compared to the bulk value (~5.24 Å). Considering that bulk GdCa has a larger lattice parameter than YSZ (5.24 Å vs. 5.14 Å), epitaxial growth on YSZ is expected to induce in-plane compressive strain in the GdCa film, and correspondingly, out-of-plane tensile strain due to the Poisson effect. Therefore, one would expect the out-of-plane lattice parameter of the film to be larger than that of the bulk. However, the slightly smaller measured value for the film might suggest that the bulk polycrystalline GdCa contains more defects such as grain boundaries and dislocations, which can artificially expand the average lattice parameter.

The in-situ temperature-dependent XRD measurements show that the fluorite structure of the GdCa film remains stable at least up to 1200 °C, with no signs of phase separation or secondary phases. To further assess thermal robustness, a separate sample was annealed at 1200 °C for one hour. The ex-situ XRD and TEM analyses confirm that the film preserves its epitaxial single-crystalline structure with only minimal interfacial diffusion, demonstrating good high-temperature structural stability (see Figure. S1 in the supplementary material). This high thermal stability is a critical advantage for applications in extreme environments. With increasing temperature, the diffraction peaks shift to lower angles due to thermal expansion. The calculated coefficient of thermal expansion (CTE) is approximately (5.2±0.3) × 10^{-6}/°C (95% confidence interval) (see more details in the supplementary material), closely matching that of YSZ (100) (~5.3 × 10^{-6} /°C), indicating good thermal compatibility between the film and substrate.

Atomic-scale High-angle annular dark-field (HAADF)-STEM coupled with energy-dispersive X-ray spectroscopy (EDS) was employed to investigate the local structure, particularly at the film–substrate interface. As shown in Fig. 2(a), the GdCa/YSZ (100) interface displays a single crystalline GaCa film and a fully coherent interface, in line with the XRD results. The EDS maps in Fig. 2(b) confirm the uniform distribution of all constituent elements within the thin film. Quantitative large-area mapping of the Hf–M, Zr–L, Ce–L, Gd–L, and Ca–K edges yielded atomic percentages of approximately 20.3 % Hf, 27.7 % Zr, 27.2 % Ce, 17.3 % Gd, and 7.5 % Ca—values close to the nominal bulk composition $(HfZrCe)_{0.25}(GdCa)_{0.125}O_{2-\delta}$. It is noted, however, that such slight deviations from target stoichiometry are common in PLD-grown multi-cation oxides.[36]

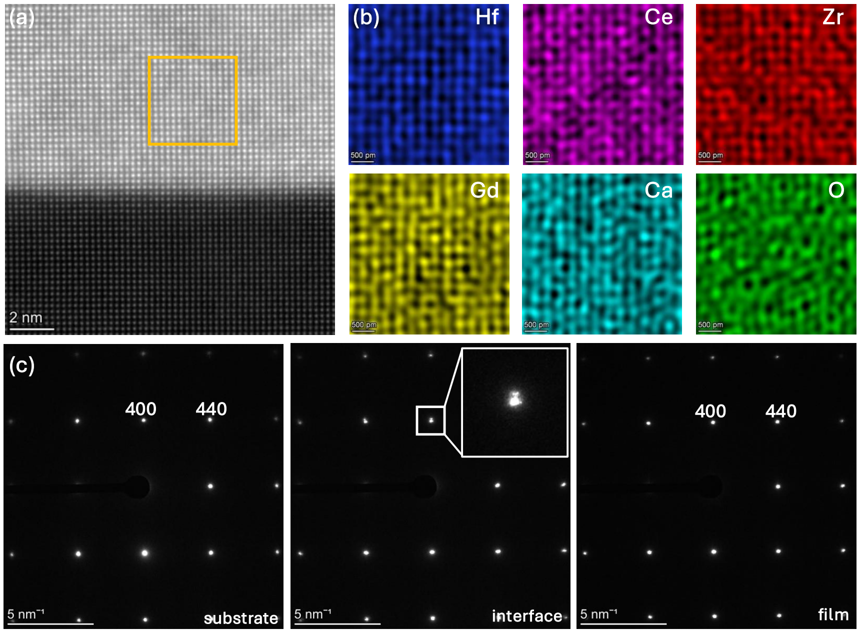

FIG. 2. TEM characterization of the chemically disordered single-phase GdCa film (top) on the YSZ (100) substrate (bottom). (a) High-resolution HAADF-STEM image showing the epitaxial growth of the GdCa film on the YSZ substrate with a coherent interface. (b) Elemental mapping confirming the homogeneous distribution of the constituent elements throughout the chemically disordered single-phase GdCa film. (c) Selected area electron diffraction (SAED) patterns obtained from the substrate, the interface, and the GdCa film, respectively.

The reduced Ca concentration is likely due to its higher volatility during film growth, where Ca species may not fully condense or may re-evaporate prior to incorporation. Conversely, Hf is refractory and has a high cohesive energy, making it more difficult to ablate. In multi-cation systems, the laser plume often diverges by mass and energy; heavier species such as Hf can ablate less efficiently or exhibit different angular distributions, leading to lower incorporation rates in the film. The calculated configuration entropy decreases marginally from 1.56 R/mol in the bulk to 1.53 R/mol in the thin film, still satisfying the high-entropy oxide criterion (>1.5 R/mol).[37]

PLEASE CITE THIS ARTICLE AS DOI: 10.1063/5.0295899

Figure 2(c) presents SAED patterns collected from the substrate, the interface, and the film. The sharp spots in both the film and substrate regions confirm their single-crystalline cubic fluorite structures. At the interface, however, the appearance of double spots perpendicular to the substrate suggests localized double diffraction and slight lattice difference between the film and substrate—due to overlapping lattice planes or interface strain.

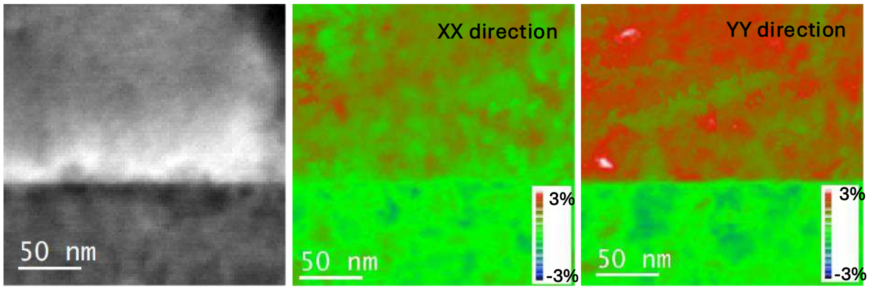

FIG. 3. Strain mapping of the chemically disordered single-phase GdCa film grown on a YSZ (100) substrate is shown in the middle and right panels for the in-plane (XX) and out-of-plane (YY) directions, respectively. The strain values are calculated using the lattice parameters of the YSZ substrate as the reference. The left panel presents a HAADF-STEM image of the corresponding region analyzed for strain, clearly depicting the interface between the GdCa thin film (top) and the YSZ substrate (bottom).

To evaluate the presence of strain, localized strain mapping was obtained on the chemically disordered single-phase GdCa film grown on a YSZ (100) substrate. As shown in Fig. 3, the in-plane (XX) strain in the film is minimal, indicating that the film is relatively well lattice-matched to the substrate in the lateral direction, though slight relaxation may occur further from the interface. In contrast, the out-of-plane (YY) strain shows a pronounced red-orange contrast—approaching +3%—across the film thickness, suggesting significant tensile strain along the growth direction. The interface is sharp but exhibits a gradual transition zone, indicating how the lattice mismatch is primarily accommodated out-of-plane. Overall, the film retains a coherent interface with the substrate while exhibiting partial relaxation, particularly away from the interface.

PLEASE CITE THIS ARTICLE AS DOI: 10.1063/5.0295899

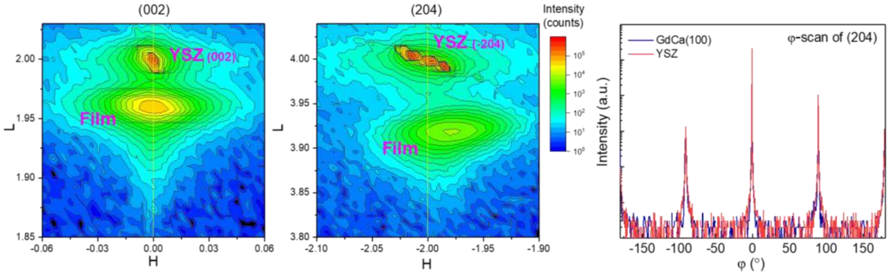

FIG. 4. RSM around (002) of chemically disordered single-phase GdCa/YSZ (100) (left panel) and RSM around (204) (middle panel). The right panel is the φ-scan of the 204 diffractions for GdCa/YSZ (100).

X-ray reciprocal space mapping (RSM) was further conducted to evaluate the epitaxial coherence and strain state of the chemically disordered single-phase GdCa film on the YSZ (100) substrate, as shown in Fig. 4. In the (002) RSM (left panel), the YSZ substrate exhibits a sharp, symmetric diffraction peak centered at H ≈ 0 and L ≈ 2.01, indicative of a high-quality, strain-free single crystal. In contrast, the GdCa film peak is broader, centered at a slightly lower L ≈ 1.97 nm^{-1} and offset along H ≈ –0.02. The broadening of the film peak suggests the presence of mosaicity or dislocations, while the downward L shift implies an expanded out-of-plane lattice parameter compared to YSZ—consistent with the tensile strain observed in strain mapping. The shift in L is also consistent with vertical lattice expansion via Poisson's effect. The lateral (H) offset between film and substrate peaks indicates that the film is not fully pseudomorphic and has undergone partial in-plane strain relaxation.

The asymmetric (204) RSM (middle panel) further confirms the tensile strain and partial relaxation. The diffraction peak centres for YSZ and GdCa in the (-204) RSM are around (-2.00, 4.00) and (-1.98, 3.91), respectively. Using the in-plane scattering vector positions, the in-plane lattice parameter of the GdCa film is estimated to be ~5.19 Å, giving a relaxation level of around 50% relative to the full mismatch between GdCa (5.24 Å) and YSZ (5.14 Å). The film and substrate peaks are clearly separated in both L and H, reinforcing the conclusion that the film has relaxed from the lattice-matched state.

The Matthews–Blakeslee model is applied to estimate the critical thickness critical thickness for the onset of strain relaxation, yielding ~10.4 nm (see more details in supplementary material).[38] As widely reported, this model is known to underestimate critical thickness in many oxide systems.[39] Nonetheless, since partial relaxation is observed in this ~63.6 nm-thick film, the actual critical thickness lies below this value for our system. We note that the critical thickness observed here is relatively smaller than those reported for other high-entropy oxides.[40,41] However, direct comparison across studies is not straightforward, as critical thickness is strongly influenced by composition, crystal structure, lattice mismatch, elastic constants, oxygen-vacancy chemistry, interface quality, PLD growth conditions, and post-growth cooling method. In our case, the relatively large tensile mismatch, possible defect-assisted strain relaxation associated with energetic PLD growth, and high oxygen-vacancy concentration that may accelerate dislocation nucleation likely contribute to the earlier onset of relaxation.

The φ-scan of the (204) reflection (right panel) reveals sharp, periodic peaks at 90° intervals (–180°, –90°, 0°, +90°, +180°) for both film and substrate, characteristic of four-fold symmetry. The close alignment of the φ-scan peaks between film and substrate confirms cube-on-cube epitaxial growth with a well-defined in-plane orientation relationship. Although the film peaks are slightly broader and weaker—indicative of some mosaic spread or domain misalignment—their sharpness attests to high crystallinity and good epitaxial quality. Together, these results confirm that the chemically disordered single-phase GdCa film is epitaxially grown on YSZ (100) with coherent interface and partial strain relaxation.

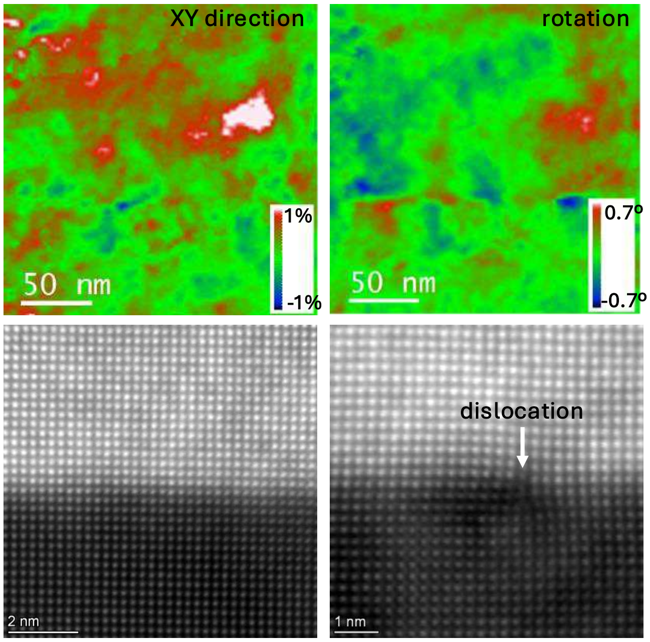

FIG. 5. Strain mapping for the chemically disordered single-phase GdCa film on YSZ (100) substrate along XY direction (upper left panel) and rotation (upper right panel). High-resolution HAADF-STEM image showing the perfect interface atomic alignment (lower left panel) and interface with atomic dislocation (lower right panel).

As shown above, the chemically disordered single-phase GdCa film grows epitaxially on the YSZ (100) substrate, resulting in matched in-plane lattice parameters. However, due to the intrinsic lattice mismatch between the GdCa film and the YSZ substrate, in-plane strain is introduced into the film. This strain is partially relieved through multiple relaxation mechanisms. As illustrated in Fig. 5, strain mapping along the in-plane (XY) direction (upper left panel) and local rotation analysis (upper right panel) reveals that portions of the film exhibit slight lattice distortion and tilting, indicative of strain relaxation processes. The high-resolution HAADF-STEM images further support this observation: while many regions show a well-aligned, coherent interface (lower left panel), dislocations are observed at certain locations along the interface (lower right panel), serving as another mechanism to relieve the strain accumulated during epitaxial growth.

In summary, we have synthesized an epitaxial chemically disordered single-phase fluorite oxide thin film, $(HfZrCeGdCa)O_2$, on a YSZ (100) substrate using pulsed laser deposition (PLD). X-ray diffraction (XRD) and high-angle annular dark-field (HAADF) atomic-resolution scanning transmission electron microscopy (STEM), combined with energy-dispersive X-ray spectroscopy (EDS), confirm the high crystalline quality of the epitaxially grown film and the uniform elemental distribution, affirming its chemically disordered single-phase nature. In-situ temperature-dependent XRD measurements reveal no secondary phase formation up to 1200 °C, indicating good thermal stability of the epitaxial chemically disordered single-phase GdCa film. Reciprocal space mapping (RSM) and strain analysis show that the in-plane lattice of the film is coherently matched to that of the YSZ substrate, while a tensile strain develops in the out-of-plane direction. Furthermore, local lattice tilting, rotation, and interfacial dislocations are observed, which likely contribute to partial strain relaxation. These findings highlight the structural robustness and epitaxial integrity of chemically disordered single-phase fluorite oxide films, paving the way for their application in advanced functional coatings, including thermally and structurally demanding environments.

Supplementary Material

See the supplementary material for the TEM and XRD characterization of the post-annealed sample, the procedure for the CTE evaluation, and the method used to estimate the critical thickness of the coating.

This research is supported by Agency for Science, Technology and Research (A*STAR) under its programs: (1) Mat-GDT (Materials − Generative Design Testing) Framework (Grant No. M24N4b0034); (2) Future Energy Acceleration & Translation (FEAT), Strategic Research & Translation Thrust (SRTT). This research used the TEM resources and facilities at Institute of

Materials Research and Engineering (IMRE), A*STAR. We thank Prof. Kedar Hippalgaonkar for the fruitful discussion.

AUTHOR DECLARATIONS

Conflict of Interest

The authors have no conflicts to disclose.

Author Contributions

J.Z. and N.L.M.W contributed equally to this work.

Jun Zhou: Conceptualization (supporting); Investigation (equal); Data curation (equal); Writing – original draft (lead). **Nancy Lai Mun Wong:** Investigation (equal); Data curation (equal); Writing – review & editing (supporting). **Hui Ru Tan:** Data curation (equal); **Ming Lin:** Data curation (equal); Formal analysis (supporting); Writing – review & editing (supporting). **Fengxia Wei:** Data curation (supporting); Formal analysis (supporting); Writing – review & editing (supporting). **Ping Yang:** Data curation (supporting); Formal analysis (supporting); Writing – review & editing (supporting). **Siao Li Liew:** Investigation (supporting); Writing – review & editing (supporting). **Jianwei Chai:** Formal analysis (supporting); Writing – review & editing (supporting). **Andrew Chun Yong Ngo:** Funding acquisition (equal); Project administration (equal); Writing – review & editing (supporting). **Shijie Wang:** Conceptualization (lead); Resources (lead); Funding acquisition (lead); Project administration (lead); Writing – original draft (supporting).

DATA AVAILABILITY

The data that support the findings of this study are available within the article.

REFERENCES

[1] C. M. Rost, E. Sachet, T. Borman, A. Moballegh, E. C. Dickey, D. Hou, J. L. Jones, S. Curtarolo, and J. P. Maria, Nat. commun. **6**, 8485 (2015).

[2] Corey Oses, Cormac Toher, and Stefano Curtarolo, Nat. Rev. Mater. **5** (4), 295 (2020).

[3] Rui-Zhi Zhang and Michael J. Reece, J. Mater. Chem. A **7** (39), 22148 (2019).

[4] W. L. Hsu, C. W. Tsai, A. C. Yeh, and J. W. Yeh, Nat Rev Chem **8** (6), 471 (2024).

[5] Yu Dong, Ke Ren, Qiankun Wang, Gang Shao, and Yiguang Wang, Journal of Advanced Ceramics **11** (1), 66 (2021).

[6] Fei Wang, Xueliang Yan, Tianyao Wang, Yaqiao Wu, Lin Shao, Michael Nastasi, Yongfeng Lu, and Bai Cui, Acta Mater. **195**, 739 (2020).

[7] Cormac Toher, Corey Oses, Marco Esters, David Hicks, George N. Kotsonis, Christina M. Rost, Donald W. Brenner, Jon-Paul Maria, and Stefano Curtarolo, MRS Bull. **47** (2), 194 (2022).

[8] Shasha Huang, Jun Zhang, Haijun Fu, Yaoxu Xiong, Shihua Ma, Xuepeng Xiang, Biao Xu, Wenyu Lu, Yanwen Zhang, William J. Weber, and Shijun Zhao, Prog. Mater Sci. **143** (2024).

[9] M. Fu, X. Ma, K. Zhao, X. Li, and D. Su, iScience **24** (3), 102177 (2021).

[10] Yingtong Pan, Ji-Xuan Liu, Tian-Zhe Tu, Wenzhong Wang, and Guo-Jun Zhang, Chem. Eng. J. **451** (2023).

[11] M. V. Kante, M. L. Weber, S. Ni, I. C. G. van den Bosch, E. van der Minne, L. Heymann, L. J. Falling, N. Gauquelin, M. Tsvetanova, D. M. Cunha, G. Koster, F. Gunkel, S. Nemsak, H. Hahn, L. Velasco Estrada, and C. Baeumer, ACS Nano **17** (6), 5329 (2023).

[12] Saeid Akrami, Parisa Edalati, Masayoshi Fuji, and Kaveh Edalati, Mater. Sci. Eng. R: Rep. **146** (2021).

[13] Xianglin Xiang, Zhong Yang, Jian Yang and Zong-Yan Zhao, Materials Futures **3**, 042103 (2024).

[14] B. Cantor, I. T. H. Chang, P. Knight, and A. J. B. Vincent, Mat. Sci. Eng. : A **375-377**, 213 (2004).

[15] Y. Yao, Q. Dong, A. Brozena, J. Luo, J. Miao, M. Chi, C. Wang, I. G. Kevrekidis, Z. J. Ren, J. Greeley, G. Wang, A. Anapolsky, and L. Hu, Science **376** (6589), eabn3103 (2022).

[16] H. Shahbazi, P. Seraji, H. Farraj, T. Yang, A. Kim, S. Fattahpour, I. Papailias, M. Diamond, S. Namvar, A. Ahmadiparidari, S. Wang, Z. Liu, S. Feng, K. Kumar, M. Ahart, J. Cabana, S. Kadkhodaei, J. Wang, Z. Huang, R. J. Hemley, and A. Salehi-Khojin, Science **388** (6750), 950 (2025).

[17] Simon Divilov, Hagen Eckert, David Hicks, Corey Oses, Cormac Toher, Rico Friedrich, Marco Esters, Michael J. Mehl, Adam C. Zettel, Yoav Lederer, Eva Zurek, Jon-Paul Maria, Donald W. Brenner, Xiomara Campilongo, Suzana Filipović, William G. Fahrenholtz, Caillin J. Ryan, Christopher M. DeSalle, Ryan J. Crealese, Douglas E. Wolfe, Arrigo Calzolari, and Stefano Curtarolo, Nature **625** (7993), 66 (2024).

[18] R. Zhang, C. Wang, P. Zou, R. Lin, L. Ma, L. Yin, T. Li, W. Xu, H. Jia, Q. Li, S. Sainio, K. Kisslinger, S. E. Trask, S. N. Ehrlich, Y. Yang, A. M. Kiss, M. Ge, B. J. Polzin, S. J. Lee, W. Xu, Y. Ren, and H. L. Xin, Nature **610** (7930), 67 (2022).

[19] B. Jiang, Y. Yu, J. Cui, X. Liu, L. Xie, J. Liao, Q. Zhang, Y. Huang, S. Ning, B. Jia, B. Zhu, S. Bai, L. Chen, S. J. Pennycook, and J. He, Science **371** (6531), 830 (2021).

[20] Y. Zeng, B. Ouyang, J. Liu, Y. W. Byeon, Z. Cai, L. J. Miara, Y. Wang, and G. Ceder, Science **378** (6626), 1320 (2022).

[21] T. L. Tan, H. M. Jin, M. B. Sullivan, B. Anasori, and Y. Gogotsi, ACS Nano **11** (5), 4407 (2017).

[22] Joshua Gild, Jeffrey Braun, Kevin Kaufmann, Eduardo Marin, Tyler Harrington, Patrick Hopkins, Kenneth Vecchio, and Jian Luo, J Materiomics. **5** (3), 337 (2019).

[23] Sicong Jiang, Tao Hu, Joshua Gild, Naixie Zhou, Jiuyuan Nie, Mingde Qin, Tyler Harrington, Kenneth Vecchio, and Jian Luo, Scripta Mater. **142**, 116 (2018).

[24] H. Xu, Z. Zhang, J. Liu, C. L. Do-Thanh, H. Chen, S. Xu, Q. Lin, Y. Jiao, J. Wang, Y. Wang, Y. Chen, and S. Dai, Nat. Commun. **11** (1), 3908 (2020).

[25] Ruzica Djenadic, Abhishek Sarkar, Oliver Clemens, Christoph Loho, Miriam Botros, Venkata S. K. Chakravadhanula, Christian Kübel, Subramshu S. Bhattacharya, Ashutosh S. Gandhi, and Horst Hahn, Materials Research Letters **5** (2), 102 (2016).

[26] Mohana V. Kante, Horst Hahn, Subramshu S. Bhattacharya, and Leonardo Velasco, J. Alloys Compd. **947** (2023).

[27]George N. Kotsonis, Saeed S. I. Almishal, Leixin Miao, Mary Kathleen Caucci, Gerald R. Bejger, Sai Venkata Gayathri Ayyagari, Tyler W. Valentine, Billy E. Yang, Susan B. Sinnott, Christina M. Rost, Nasim Alem, and Jon-Paul Maria, Appl. Phys. Lett. **124** (17) (2024).

[28]Joshua Gild, Mojtaba Samiee, Jeffrey L. Braun, Tyler Harrington, Heidy Vega, Patrick E. Hopkins, Kenneth Vecchio, and Jian Luo, J. Eur. Ceram. Soc. **38** (10), 3578 (2018).

[29]Robert Vassen, Xueqiang Cao, Frank Tietz, Debabrata Basu, and Detlev Stöver, J. Am. Ceram. Soc. **83** (8), 2023 (2004).

[30]Kepi Chen, Xintong Pei, Lei Tang, Haoran Cheng, Zemin Li, Cuiwei Li, Xiaowen Zhang, and Linan An, J. Eur. Ceram. Soc. **38** (11), 4161 (2018).

[31]Siao Li Liew, Nafisah Bte Mohd Rafiq, Xi Ping Ni, Sze Yu Tan, Poh Chong Lim, and Shijie Wang, J. Alloys Compd. **1004** (2024).

[32]Siao Li Liew, Xi Ping Ni, Fengxia Wei, Sze Yu Tan, Meng Tzee Luai, Poh Chong Lim, Siew Lang Teo, Nafisah Bte Mohd Rafiq, Jun Zhou, and Shijie Wang, J. Eur. Ceram. Soc. **42** (14), 6608 (2022).

[33]Siao Li Liew, Jun Zhou, Fengxia Wei, Xi Ping Ni, Sze Yu Tan, Poh Chong Lim, Meng Tzee Luai, Jing Jun Coryl Lee, Ming Yang, and Shijie Wang, J. Alloys Compd. **904**, 164097 (2022).

[34]S. L. Liew, N. B. M. Rafiq, X. P. Ni, A. Sng, P. C. Lim, J. Zhou, and S. Wang, Inorg. Chem. **64** (4), 1726 (2025).

[35]Zhibo Zhao, Moaz Waqar, Arun Kumar Jaiswal, Aaditya Rangan Raghavan, Dirk Fuchs, Jing Lin, Torsten Brezesinski, Subramshu S. Bhattacharya, Horst Hahn, Xiaoqing Pan, Robert Kruk, and Abhishek Sarkar, Appl. Phys. Lett. **125** (1) (2024).

[36]Alejandro Ojeda-G-P, Christof W. Schneider, Max Döbeli, Thomas Lippert, and Alexander Wokaun, Appl. Surf. Sci. **389**, 126 (2016).

[37]Andrew J. Wright, Qingyang Wang, Chuying Huang, Andy Nieto, Renkun Chen, and Jian Luo, J. Eur. Ceram. Soc. **40** (5), 2120 (2020).

[38]J. W. Matthews and A. E. Blakeslee, J. Cryst. Growth **32** (2), 265 (1976).

[39]E. A. Fitzgerald, G. P. Watson, R. E. Proano, D. G. Ast, P. D. Kirchner, G. D. Pettit, and J. M. Woodall, J. Appl. Phys. **65** (6), 2220 (1989).

[40]S. S. I. Almishal, P. Kezer, J. T. Sivak, Y. Iwabuchi, S. V. G. Ayyagari, S. Sarker, M. Furst, G. Bejger, B. Yang, S. Gelin, N. Alem, I. Dabo, C. M. Rost, S. B. Sinnott, V. Crespi, V. Gopalan, R. Engel-Herbert, J. T. Heron, and J. P. Maria, Adv Sci (Weinh), e09868 (2025).

[41]Saeed S. I. Almishal, Leixin Miao, Yueze Tan, George N. Kotsonis, Jacob T. Sivak, Nasim Alem, Long-Qing Chen, Vincent H. Crespi, Ismaila Dabo, Christina M. Rost, Susan B. Sinnott, and Jon-Paul Maria, J. Am. Ceram. Soc. **108** (2) (2024).